Pathological mechanism of ferroptosis in a rat model of α-naphthyl isothiocyanate-induced chronic cholestasis

ZHEN GUO[1,2*], JIAXUAN WANG[2,3*], YIWEN WANG[2], XINZHU LIU[2], YUBING XIA[2,3], PING LIU[2], LI QI[2], JIA LIU[2] and XIAONING WANG[2]

[1]Luzhou Key Laboratory of Research and Development of Medical Institution Preparations and Large-Scale Health Products, The Affiliated Traditional Chinese Medicine Hospital, Southwest Medical University, Luzhou, Sichuan 646000, P.R. China; [2]Institute of Interdisciplinary Science, Shanghai University of Traditional Chinese Medicine, Shanghai 201203, P.R. China; [3]Department of Hepatology, Yueyang Hospital of Integrated Traditional Chinese and Western Medicine, Shanghai University of Traditional Chinese Medicine, Shanghai 200071, P.R. China

Received May 22, 2025; Accepted December 18, 2025

DOI: 10.3892/mmr.2026.13802

Abstract. Ferroptosis is an iron-dependent form of cell death associated with liver pathologies. However, its role in chronic cholestasis remains to be fully elucidated. The present study therefore investigated the pathological mechanism of ferroptosis in a rat model of α-naphthyl isothiocyanate (ANIT)-induced chronic cholestasis and evaluated the therapeutic potential of the iron chelator deferoxamine (DFO). Wistar rats were used to establish a chronic cholestasis model via ANIT administration, with a subset of animals receiving DFO treatment. Wistar rats that were subjected to chronic ANIT exposure were found to develop severe liver injury, characterized by impaired function, inflammation and fibrosis. In addition, pronounced iron deposition and hallmark features of ferroptosis, including elevated lipid peroxidation, depleted glutathione, and aberrant expression of acyl-CoA synthetase long-chain family member 4 and cyclooxygenase 2, were observed. Ultrastructural analysis revealed distinctive mitochondrial abnormalities consistent with ferroptosis. Mechanistically, these changes appeared to be mediated by suppression of the Kelch-like ECH-associated protein 1/nuclear factor erythroid 2-related factor 2/heme oxygenase 1 antioxidant pathway and dysregulation of key iron metabolism proteins, including transferrin receptor 1 and ferroportin 1. Intervention with DFO markedly ameliorated the cholestatic injury, reduced iron overload and lipid peroxidation, mitigated mitochondrial damage, and normalized the expression of key proteins involved in ferroptosis, antioxidant defense and iron homeostasis. Taken together, these findings suggested that ferroptosis may be a key pathological mechanism in chronic cholestasis, driven by the concurrent disruption of antioxidant and iron metabolic capacities in hepatocytes. Therefore, targeting iron overload may be a promising therapeutic strategy for cholestasis.

Correspondence to: Professor Xiaoning Wang, Institute of Interdisciplinary Science, Shanghai University of Traditional Chinese Medicine, 1200 Cailun Road, Zhangjiang Hi-Tech Park, Pudong New District, Shanghai 201203, P.R. China
E-mail: wxntcm@126.com

*Contributed equally

Key words: ferroptosis, chronic cholestasis, antioxidant, iron deposition, reactive oxygen species

Introduction

Cholestasis is characterized by the obstruction of bile formation, secretion and excretion in hepatocytes or bile duct epithelial cells, due to various intrahepatic or extrahepatic causes. This condition prevents bile from entering the duodenum and results in its direct entry into the bloodstream (1,2). A previous study indicated that 35% patients newly diagnosed with chronic liver disease will typically develop cholestasis (3). Cholestasis presents as initial clinical assessments revealing elevated serum alkaline phosphatase (ALP) and γ-glutamyl transferase (GGT) activity; however, 56% of patients do not achieve normal serum biochemical levels of ALP and GGT upon discharge (4). Without appropriate treatment, these abnormalities can substantially increase the risk of hyperbilirubinemia, liver fibrosis, cirrhosis and liver failure, posing a notable threat to patient survival (5). Therefore, investigating safe and effective treatments for cholestasis is of clinical importance.

Ferroptosis, first identified by Dixon *et al* (6) in 2012, is a form of cell death characterized by iron and reactive oxygen species (ROS) involvement. Unlike traditional cell death mechanisms, ferroptosis results from iron-dependent lipid peroxidation and exhibits distinct ultrastructural features. Elevated lipid peroxidation levels serve as a key indicator of ferroptosis occurrence (7).

Persistent cholestasis exacerbates damage to bile duct epithelial cells and hepatocytes, triggering an inflammatory response (8). Inflammation is strongly associated with

oxidative stress (9,10). During inflammation, pro-inflammatory factors stimulate phagocytes and non-phagocytic cells to produce various ROS, such as O^{2-}, H_2O_2 and OH^-, to eliminate pathogens (11). Excessive intracellular ROS then overwhelm glutathione peroxidase 4 (GPX4), disrupting the balance between ROS production and scavenging, leading to ferroptosis (12). Additionally, inflammatory changes in hepatocytes, including chronic viral hepatitis, acute hepatitis and cholestatic hepatitis, can cause intracellular ferritin efflux (13). Ferritin binds Fe^{2+}, whereas its depletion increases free Fe^{2+} levels. Excess Fe^{2+} can react with H_2O_2 through the Fenton reaction, producing OH^- and hydroxyl radicals with strong oxidizing properties, thereby promoting ferroptosis (14). Therefore, molecules and signals involved in iron metabolism and lipid peroxidation are crucial in the initiation and progression of ferroptosis (15).

The specific link between α-naphthyl isothiocyanate (ANIT)-induced cholestasis and iron metabolism dysregulation warrants emphasis. Chronic cholestasis is associated with a persistent inflammatory response, which can disrupt the hepatic expression of hepcidin, a master regulator of iron homeostasis (16,17). Reduced hepcidin levels can lead to increased iron absorption and mobilization, resulting in hepatic iron overload (18). This iron-rich environment, coupled with ANIT-induced oxidative stress, creates a favorable condition for the Fenton reaction and lipid peroxidation, thereby priming hepatocytes for ferroptosis (19,20).

Hepatic stellate cells (HSCs) remain quiescent in healthy liver. By contrast, upon cholestatic liver damage, persistent intrahepatic inflammation can activate HSCs, transforming them from vitamin A-storing cells into proliferative, contractile, inflammatory and chemotactic myofibroblasts that produce extracellular matrix proteins (21). Ferroptosis in hepatocytes accelerates this transformation (22). Following ferroptosis activation, hepatocytes lose their normal functions, weakening their inhibitory effect on nearby HSCs. The release of free iron ions and ROS from dead hepatocytes further stimulates HSC activation, perpetuating ferroptosis. This vicious cycle exacerbates inflammation, enhances HSC activation and increases extracellular matrix synthesis, including type IV collagen and laminin, thereby advancing cholestatic disease progression (23).

Deferoxamine (DFO) is a Food and Drug Administration-approved iron chelator that has been extensively applied for treating iron overload disorders such as β-thalassemia and myelodysplastic syndrome (24). It can effectively reduce free iron ion levels by chelating them within cells to directly inhibit the Fenton reaction, thereby preventing cell ferroptosis (25).

Given the intrinsic link between cholestasis and ferroptosis, it has been hypothesized that hepatocyte ferroptosis serves as a key driver in the progression of chronic cholestasis. Therefore, the present study aimed to assess this hypothesis using the iron chelator DFO to investigate whether the inhibition of ferroptosis through iron chelation could attenuate the progression of chronic cholestatic liver injury.

Materials and methods

Animal models and experimental design

Animal welfare and ethical considerations. All animal experiments were approved by the Animal Care and Utilization Committee of Shanghai University of Traditional Chinese Medicine (approval no. PZSHUTCM210715019; Shanghai, China) and were conducted in strict accordance with the National Institutes of Health Guide for the Care and Use of Laboratory Animals (26).

Animal housing. A total of 24 6-week-old male Wistar rats (batch no. 0054518) were purchased from Shanghai SLAC Laboratory Animal Co., Ltd. [license no. SCXK (Shanghai) 2017-0005]. The rats weighed 160-180 g upon arrival. They were housed under specific pathogen-free conditions at 23-24˚C with 60±10% humidity, under a 12-h light/12-h dark cycle. After 1 week of acclimation, the rats were randomly divided into a control group (n=8) and a model group (n=16).

Dosages. The control group received daily intragastric administration of an equivalent volume of olive oil (3 ml/kg) and standard laboratory chow diet. The model group received intragastric administration of a 2% ANIT (Sigma-Aldrich; Merck KGaA)-olive oil solution (3 ml/kg) every other day (27) for 12 weeks. From week 9, the model group was subdivided into the ANIT (n=8) and DFO-treated (n=8) groups. The DFO-treated group received daily DFO treatment (MedChemExpress; 100 mg/kg) (28) for 4 weeks (weeks 9-12). All animals were sacrificed at the end of week 12 (Fig. 1).

Health monitoring and humane endpoints. The health and behavior of all animals were monitored at least twice daily (morning and evening) throughout the study. Pre-established humane endpoints were strictly adhered to in order to minimize suffering. Any animal exhibiting one or more of the following severe clinical signs was sacrificed immediately: i) >20% loss of initial body weight; ii) prolonged lethargy or inability to reach food or water; iii) signs of severe pain or distress (such as persistent vocalization, self-mutilation); iv) severe dyspnea or cyanosis; v) paralysis or other neurological deficits that impeded normal mobility. No animals reached these endpoints prior to the scheduled termination.

Euthanasia, anesthesia and terminal blood collection. At the end of week 12, all animals were euthanized for terminal blood collection and tissue harvesting. Euthanasia was performed by intraperitoneal injection of an overdose of sodium pentobarbital (150 mg/kg). A total of 6-8 ml of blood was aseptically collected from the inferior vena cava. Death was confirmed by the absence of a heartbeat and cessation of respiration

Analgesia. No additional analgesics were administered during the chronic model establishment, as the ANIT-induced injury is not considered to cause notable pain that requires such intervention and the administration of analgesics could potentially interact with the study endpoints. Following confirmation of death, liver tissue was harvested for subsequent analysis.

Biochemical analysis

Detection method of serum liver function and blood lipids. Blood was collected from the inferior vena cava and centrifuged (1,000 x g, 20 min and 4˚C) to obtain the serum. Serum alanine aminotransferase (ALT) (cat. no. KF749; Fujifilm Wako Pure Chemical Corporation), aspartate aminotransferase (AST; cat. no. KK718; Fujifilm Wako Pure Chemical Corporation), ALP (cat. no. EH360; Fujifilm Wako Pure Chemical Corporation) and GGT (cat. no. 010260; Yantai Ausbio Biotechnology Co., Ltd.) activities, as well as total bilirubin (TBIL; cat. no. KK678; Fujifilm Wako Pure Chemical

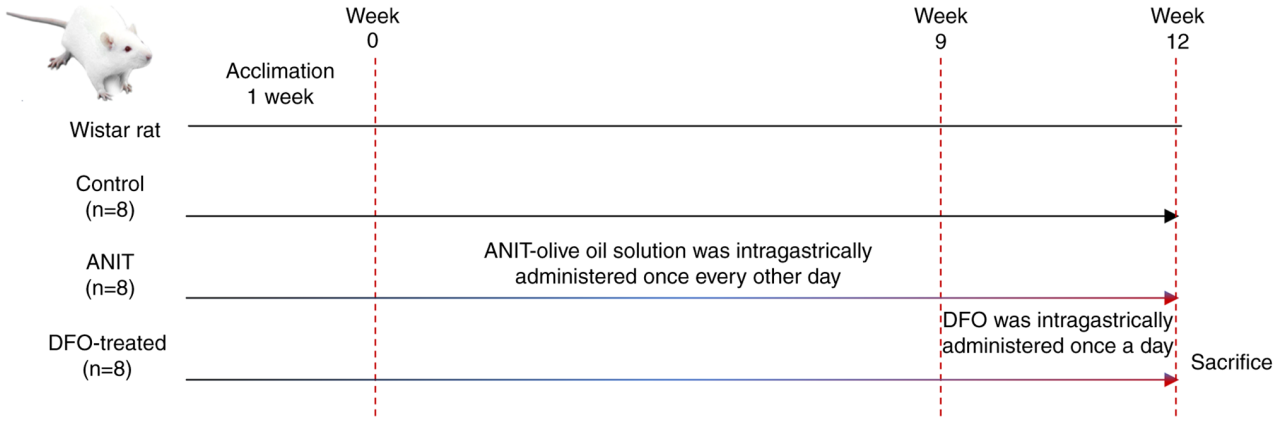

Figure 1. Schematic diagram of the experiment. ANIT, α-naphthyl isothiocyanate; DFO, deferoxamine.

Corporation), direct bilirubin (DBIL; cat. no. FF870; Fujifilm Wako Pure Chemical Corporation), total bile acid (TBA; cat. no. 210428; Yantai Ausbio Biotechnology Co., Ltd.), triglyceride (TG) (cat. no. L068; Sekisui Medical Co., Ltd.), total cholesterol (TCH) (cat. no. L979; Sekisui Medical Co., Ltd.) and low-density lipoprotein (LDL) (cat. no. EG582; Fujifilm Wako Pure Chemical Corporation) were measured using the automatic biochemical analyzer (TK-40FR; Canon Medical Systems Corporation).

Detection method of iron ions in serum and the liver. For serum analysis, 500 µl serum was introduced into the measurement tube, whereas 500 µl double-distilled water was placed in the blank tube. A standard application solution (500 µl; Iron Assay Kit (cat. no. ab83366; Abcam) was added to the standard tube. Subsequently, 1.5 ml iron chromogenic reagent was added to each tube according to the manufacturer's instructions and the tubes were incubated at 100˚C for 5 min, before being allowed to return to room temperature. Subsequently, the samples were centrifuged at 1,500 x g for 10 min at room temperature. The optical density (OD) was measured at 520 nm using a microplate reader (Infinite M200 PRO; Tecan Group, Ltd.) and the total iron concentration was calculated based on the standard curve and is expressed as mM. Briefly, the iron content (in nmol) derived from the standard curve was divided by the sample volume (500 µl) and multiplied by the sample dilution factor.

Liver tissue samples (10 mg) were homogenized in 90 µl iron assay buffer (cat. no. ab83366; Abcam) and centrifuged at 16,000 x g for 10 min, according to the manufacturer's instructions. The supernatant was transferred to a 96-well plate. For standard wells, 100 µl standard diluent was added, whereas sample wells received 35 µl sample and 65 µl iron assay buffer. Each well was treated with 5 µl iron reducing agent, followed by the addition of 100 µl iron probe after a 30-min incubation at 37˚C. Following incubation at 37˚C for 60 min in the dark, the absorbance was measured at 520 nm at room temperature. A standard curve was generated from the OD values of the standard wells and total iron content in the sample wells was calculated accordingly. To measure Fe^{2+} content, 100 µl standard diluent and 5 µl iron reducing agent were added to the standard wells, whereas 35 µl sample and 70 µl iron analysis buffer were added to the sample wells, with all other conditions unchanged.

Detection method of hydroxyproline (HYP) in the liver. Liver tissue samples (70 mg) were homogenized in 1 ml RIPA buffer (cat. no. SD006; Shanghai Sidings BioTech Co., Ltd.). Following hydrolysis at 95˚C for 20 min, 10 µl indicator was added, and the pH was adjusted until the solution turned yellow-green. The volume of each tube was then increased to 10 ml with double-distilled water; from this, 4 ml diluted hydrolysate was combined with 20 mg activated carbon and centrifuged at 1,500 x g for 10 min at room temperature. A 1-ml aliquot of the supernatant was then used as the measurement sample. For controls, 1 ml double-distilled water was added to the blank tube, with 1 ml standard solution to the standard tube. Each tube then received 0.5 ml reagents 1, 2 and 3, was mixed thoroughly and was incubated at 60˚C for 15 min. After centrifuging at 1,500 x g for 10 min at room temperature, 200 µl supernatant was taken to measure the OD at 550 nm (cat. no. A030-2; Nanjing Jiancheng Bioengineering Institute).

Detection method of malondialdehyde (MDA) in the liver. Liver tissue samples were accurately weighed (50 mg) and homogenized in 450 µl 0.9% NaCl, followed by centrifugation at 16,000 x g for 10 min at 4˚C. The supernatant was collected for protein concentration analysis using the BCA method. A working solution was prepared according to the manufacturer's instructions (cat. no. A003-1; Nanjing Jiancheng Bioengineering Institute), and 4 ml was added to each tube. To the blank tube, 1 ml absolute ethanol was added, whereas 1 ml standard solution was added to the standard tube. To the assay tube, 1 ml sample was added. The tubes were then incubated in a 95˚C water bath for 40 min, cooled to room temperature and centrifuged at 2,000 x g for 10 min at room temperature. The OD was measured at 532 nm. The MDA content in liver tissue was calculated and expressed as nmol/mg of protein (nmol/mg prot) based on the measured OD values and the known standard concentration (10 nmol/ml), normalized to the protein concentration of the tissue homogenate (cat. no. A003-1; Nanjing Jiancheng Bioengineering Institute).

Detection method of glutathione (GSH) in the liver. Liver GSH content was determined using a commercial Glutathione Assay kit (cat. no. A006-2-1; Nanjing Jiancheng Bioengineering Institute). Liver tissues were processed as aforementioned for the MDA assay. Subsequently, 60 µl reagent 1 was added to the blank well, whereas 60 µl standard was added to the

standard well and 60 μl sample was added to the assay well; 60 μl reagent 2 and 15 μl reagent 3 were then added to each well. The mixtures were allowed to form natural precipitates for 5 min at 37˚C, before the OD was measured at 405 nm. The GSH concentration was calculated according to the manufacturer's instructions.

Detection method of glutathione peroxidase (GSH-PX) in the liver. GSH-PX activity was determined using a commercial Glutathione Peroxidase Assay kit (cat. no. A005; Nanjing Jiancheng Bioengineering Institute). The liver tissues were processed as aforementioned for the MDA assay. To the non-enzymatic tube, 40 μl 1 mmol/l GSH was added, whereas 20 μl 1 mmol/l GSH and 20 μl homogenate were added to the enzymatic tube. Following the enzymatic reaction, 200 μl supernatant was extracted for the colorimetric reaction. In total, 200 μl GSH standard solvent was added to the blank tube, 200 μl 20 μmol/l GSH standard solution was added to the standard tube and 200 μl supernatant was added to both the non-enzymatic and enzymatic tubes. To each tube, 200 μl reagent 3, 50 μl reagent 4 and 10 μl reagent 5 were added. After allowing natural sedimentation for 15 min at 37˚C, the OD value was measured at 412 nm.

Histopathological evaluation. Liver tissues were sectioned into 0.5x0.5 cm pieces, fixed in 4% paraformaldehyde at room temperature for 24-48 h. The fixed tissue was dehydrated through a graded ethanol series, cleared in xylene, and embedded in paraffin. Subsequently, 4-μm thick sections were prepared. H&E staining was performed according to standard protocols. Sirius red and Prussian blue staining were performed according to the manufacturers' instructions, with incubations at room temperature (1 h for Sirius red and 30 min for Prussian blue). Digital slide scanning and panoramic imaging of all stained sections were conducted using a Panoramic Scanning and Analysis System (LEICA SCN 400; Leica Microsystems GmbH, Germany) equipped with its Leica SCN Slide Scanner Software, version 2.5; Leica Microsystems). For quantitative analysis of collagen deposition, the Sirius red-positive area (representing collagen fibers) was measured in five randomly selected fields of view/section at 200x magnification using ImageJ software (version 2.14.0; National Institutes of Health). The collagen-positive area ratio was calculated as (Sirius red-positive area/total tissue area) x100%. Similarly, the Prussian blue-positive area (representing iron deposition) was quantified (five random fields at 200x magnification), and the iron deposition-positive area ratio was calculated.

Ultrastructural pathology evaluation. Liver tissue was sectioned into 0.1x0.1 cm pieces and fixed in 2.5% glutaraldehyde at 4˚C for 4-6 h. Samples underwent standard dehydration through a graded ethanol series, followed by embedding in acetone overnight. Subsequently, 50-nm ultrathin sections were subjected to double staining with 3% uranyl acetate and lead citrate at room temperature, each for 15-20 min. The samples were examined using a transmission electron microscope (TK-40FR; FEI; Thermo Fisher Scientific, Inc.). Image acquisition and initial analysis were performed using the microscope's proprietary software (Tecnai Imaging and Analysis (TIA) Software, version 4.7; FEI/Thermo Fisher Scientific).

Western blot analysis. Liver tissue lysates were prepared using ice-cold RIPA Lysis Buffer (cat. no. SD006) supplemented with a protease inhibitor cocktail (cat. no. SD001; both Shanghai Sidings BioTech Co., Ltd.). Protein concentrations were measured using a BCA protein assay kit. Equal protein amounts (20 μg/lane) were separated by SDS-PAGE on 10%, 7.5%, or 12.5% polyacrylamide gels and transferred to nitrocellulose membranes The membranes were blocked at room temperature for 15 min using QuickBlock™ Western blocking solution (cat. no. P0239; Beyotime Biotechnology). The membranes were then incubated overnight at 4˚C with primary antibodies as follows: anti-Nrf2 (1:1,000), anti-COX2 (1:1,000), anti-GPX4 (1:5,000), anti-TFR1 (1:5,000), anti-ASCL4 (1:50,000), anti-HO-1 (1:50,000), anti-Steap3 (1:10,000), anti-α-SMA (1:2,000), anti-FPN1 (1:1,000), anti-DMT1 (1:1,000), anti-FTH1 (1:2,000), anti-XCT (1:2,000), and anti-Keap1 (1:2,000). This was followed by a 1 h incubation at room temperature with horseradish peroxidase-conjugated secondary antibodies (goat anti-rabbit IgG, cat. no. A0208, and goat anti-mouse IgG, cat. no. A0216; Beyotime Institute of Biotechnology; 1:1,000). β-actin (1:10,000; cat. no. 66009-1; Proteintech) served as an internal control. Antibodies against nuclear factor erythroid-2-related factor 2 (Nrf2; cat. no. ab137550), cyclooxygenase 2 (COX2; cat. no. ab52237), GPX4 (cat. no. ab125066), transferrin receptor 1 (TFR1; cat. no. ab269513), acyl-CoA synthetase long-chain family member 4 (ASCL4; cat. no. ab155282), heme oxygenase 1 (HO-1; cat. no. ab68477), six-transmembrane epithelial antigen of the prostate 3 (Steap3; cat. no. ab151566) and α-smooth muscle actin (α-SMA; cat. no. ab7817) were purchased from Abcam. Ferroportin 1 (FPN1; cat. no. 26601-1-AP) and divalent metal transporter 1 (DMT1; cat. no. 20507-1-AP) antibodies were purchased from Proteintech Group, Inc. Ferritin heavy chain 1 (FTH1; cat. no. PA4412) and cystine/glutamate transporter (XCT; cat. no. T57046) antibodies were purchased from Abmart Pharmaceutical Technology Co., Ltd. The Kelch-like ECH-associated protein 1 (Keap1) antibody (cat. no. bs-3648R) was purchased from BIOSS. Protein bands were visualized using Clarity Western ECL Substrate (cat. no. 1705061; Bio-Rad Laboratories, Inc.). Images of the blots were then captured and the band intensities were semi-quantified using ImageJ software (version 1.54p; National Institutes of Health).

Statistical analysis. The sample size (n=8 per group) was determined *a priori* using a power analysis conducted with G*Power software (version 3.1.9.7; gpower.hhu.de/). The effect size was estimated from preliminary data obtained from a pilot experiment with 6 rats/group, with an α level of 0.05 (two-sided) and a power (1-β) of 0.8, ensuring adequate statistical power to detect significant effects. All data are presented as the mean ± standard deviation. The normality of data distribution was confirmed using the Shapiro-Wilk test, and the homogeneity of variances was verified using Levene's test. For data that satisfied both assumptions, one-way ANOVA was performed, followed by Tukey's honestly significant difference post hoc test for multiple comparisons. For data that violated the assumption of normality or homogeneity of variances, the non-parametric Kruskal-Wallis test was applied, followed by Dunn's post hoc test for multiple comparisons. All statistical analyses were performed using SPSS software (version 25.0;

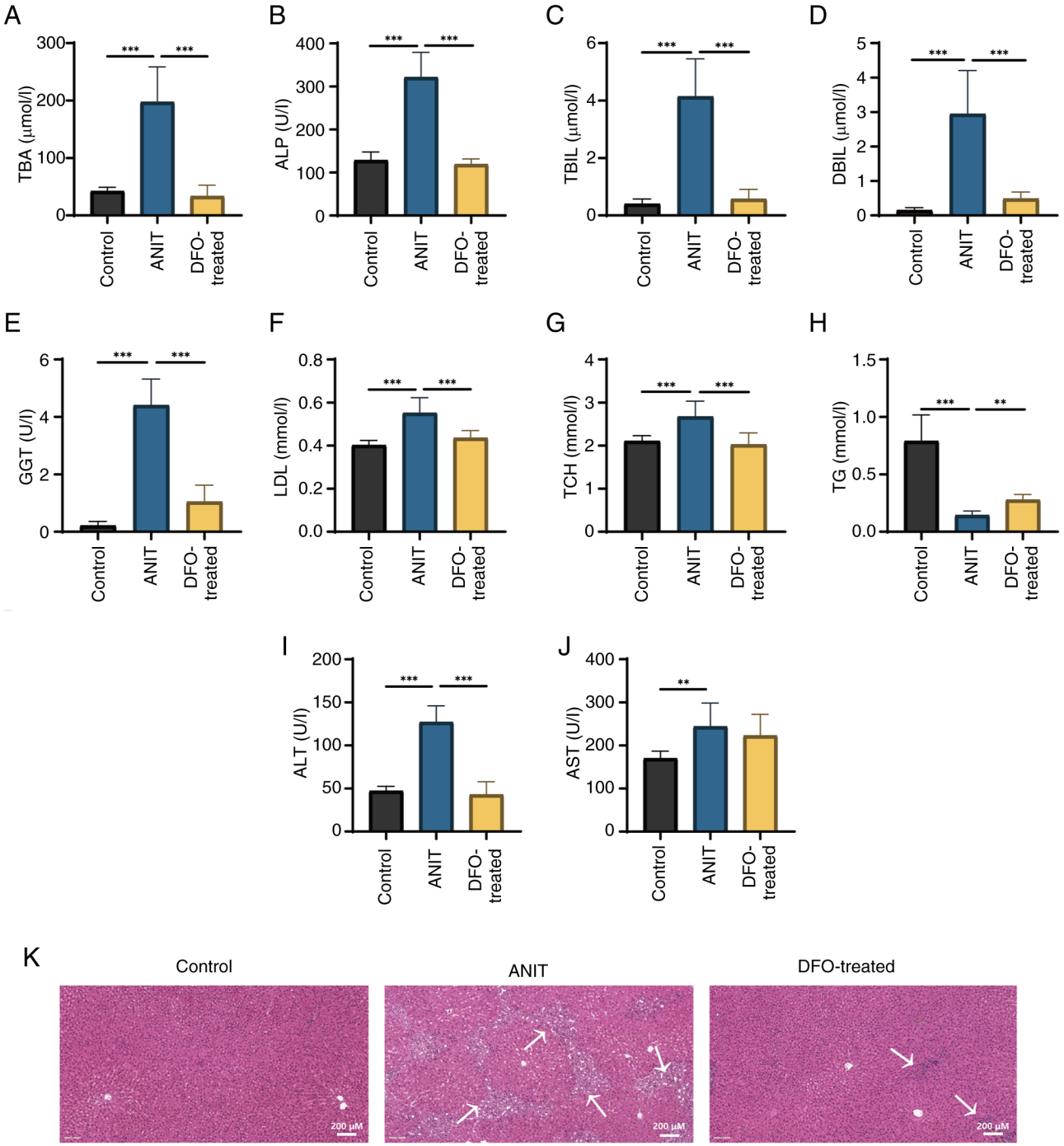

Figure 2. Liver function of rats with chronic cholestasis is impaired and histopathological analysis of liver tissue reveals inflammation. The control group was fed a chow diet, and the ANIT and DFO-treated groups were intragastrically administered ANIT olive oil solution with or without DFO (n=8/group). (A) TBA, (B) ALP, (C) TBIL, (D) DBIL, (E) GGT, (F) LDL, (G) TCH, (H) TG, (I) ALT and (J) AST were measured. **P<0.01, ***P<0.001. (K) Hematoxylin and eosin staining (scale bar, 200 μm). Arrows indicate bile duct hyperplasia and inflammatory cell infiltration in the portal area. ANIT, α-naphthyl isothiocyanate; DFO, deferoxamine; TBA, total bile acid; ALP, alkaline phosphatase; TBIL, total bilirubin; DBIL, direct bilirubin; GGT, γ-glutamyl transferase; LDL, low-density lipoprotein; TCH, total cholesterol; TG, triglyceride; ALT, alanine aminotransferase; AST, aspartate aminotransferase.

IBM Corp.). P<0.05 was considered to indicate a statistically significant difference.

Results

Liver function of rats with chronic cholestasis is impaired and histopathological examination of liver tissue reveals inflammation. ANIT-induced cholestasis led to significant increases in serum ALT, AST, ALP and GGT activities, and TBIL, DBIL, TBA, TCH and LDL levels, whereas TG levels were significantly decreased compared with those in the control group (Fig. 2A-J). DFO significantly restored serum ALT, ALP and GGT activities, and TBIL, DBIL, TBA, TCH, LDL and TG levels, compared with those in the ANIT group. H&E staining revealed bile duct hyperplasia and inflammatory cell infiltration in the portal area of

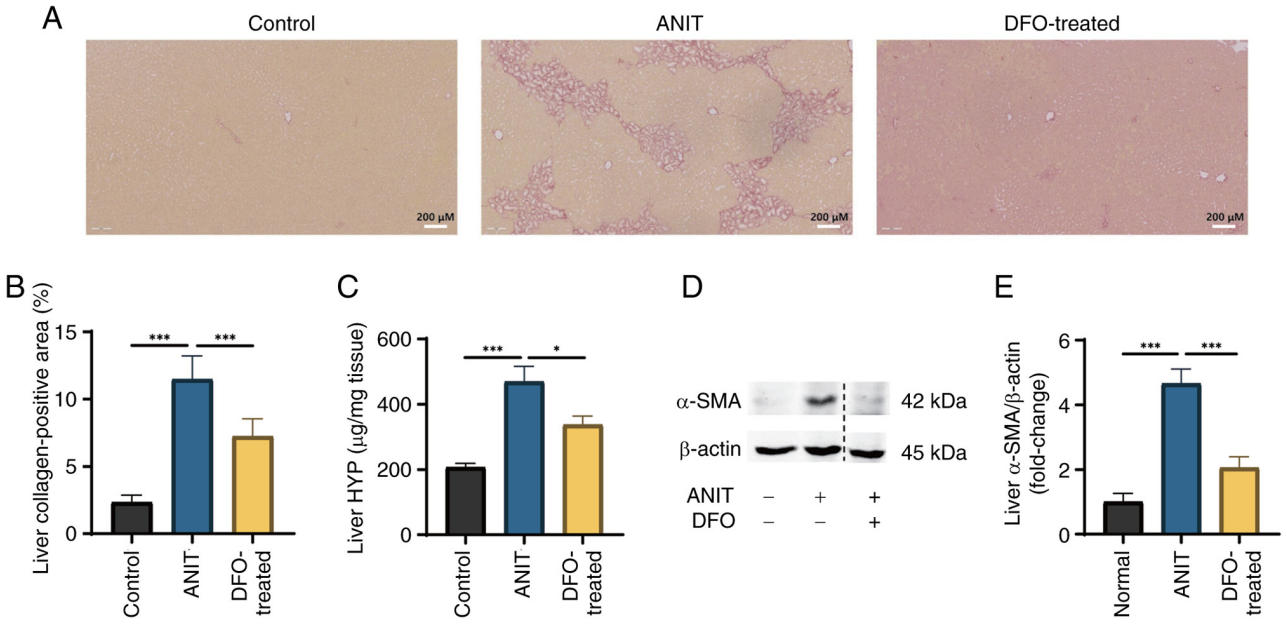

Figure 3. Intrahepatic collagen fiber deposition is increased in rats with chronic cholestasis. Control group was fed a chow diet, whereas ANIT and DFO-treated groups were intragastrically administered ANIT olive oil solution with or without DFO (n=8/group). (A) Sirius red staining (scale bar, 200 μm) and (B) collagen-positive area in the liver. (C) HYP levels in the liver. (D) Changes in α-SMA protein expression. The blots shown are representative of three independent experiments. The dotted line indicates that the lanes were non-adjacent on the original gel. (E) Relative expression levels of α-SMA. Results Data are presented as the mean ± SD. P-values were determined by one-way ANOVA. *P<0.05, ***P<0.001. ANIT, α-naphthyl isothiocyanate; DFO, deferoxamine; HYP, hydroxyproline; α-SMA, α-smooth muscle actin.

rats in the ANIT group, which were markedly inhibited by DFO treatment (Fig. 2K).

Intrahepatic collagen fiber deposition is increased in rats with chronic cholestasis. Sirius red staining revealed significant collagen fiber deposition at the periphery of rat hepatic lobules following ANIT-induced cholestasis (Fig. 3A and B). DFO treatment, by reducing iron overload, was shown to markedly improve ductular function and inflammatory cell infiltration (Fig. 2K, while significantly reducing intrahepatic collagen fiber deposition; as evidenced by a decreased Sirius red-positive staining area ratio (Fig. 3A and B). HYP levels were significantly elevated in samples from rats with ANIT-induced cholestasis compared with those in the control group, whereas DFO treatment substantially restored HYP levels (Fig. 3C). Furthermore, liver α-SMA protein expression was significantly increased in the ANIT group, whereas it was significantly reversed by DFO treatment (Fig. 3D and E).

Free iron ions in serum and liver are aberrantly increased in rats with chronic cholestasis. Serum total iron, liver total iron and Fe^{2+} content were significantly elevated in rats with ANIT-induced cholestasis compared with those in the control group; however, DFO treatment significantly decreased these levels compared with those in the ANIT group (Fig. 4A-C). Furthermore, DFO treatment significantly reduced hepatic iron deposition, as evidenced by the decreased positive Prussian blue staining area ratio (Fig. 4D). Prussian blue staining revealed extensive blue staining in the liver of rats with chronic cholestasis, indicating increased iron deposition (Fig. 4E).

Lipid peroxidation and ferroptosis marker levels are increased in the livers of rats with and the liver ultrastructure is affected in a DFO-reversible manner. In rats with ANIT-induced cholestasis, liver MDA levels were significantly increased, whereas GSH content and GSH-PX activity were significantly decreased, compared with those in the control group (Fig. 5A-C). DFO treatment, through its iron-chelating action, notably restored liver GSH-PX activity and MDA and GSH levels compared with those in the ANIT group. Furthermore, the protein expression levels of ASCL4 and COX2 were significantly elevated in the liver of rats with ANIT-induced cholestasis compared with those in the control group (Fig. 5D-F). By contrast, DFO treatment significantly reversed the aberrant expression of these aforementioned ferroptosis markers compared with those in the ANIT group. Transmission electron microscopy revealed that hepatocytes from rats with chronic cholestasis exhibited intact nuclei but characteristic mitochondrial abnormalities, including reduced size, blurred and fused cristae, and increased bilayer membrane density (Fig. 5G). By contrast, DFO-treated rats exhibited intact hepatocyte nuclei and morphologically normal mitochondrial cristae. Furthermore, the mitochondrial size in the DFO group appeared increased compared with that in the ANIT group, indicating a partial restoration of mitochondrial morphology towards a normal state.

Abnormal expression of antioxidant and iron metabolism-related proteins in liver samples of rats with chronic cholestasis. In rats with ANIT-induced cholestasis, liver protein expression levels of Nrf2, XCT and GPX4 were significantly reduced, whereas those of Keap1 and HO-1 were increased, compared with those in rats in the control group

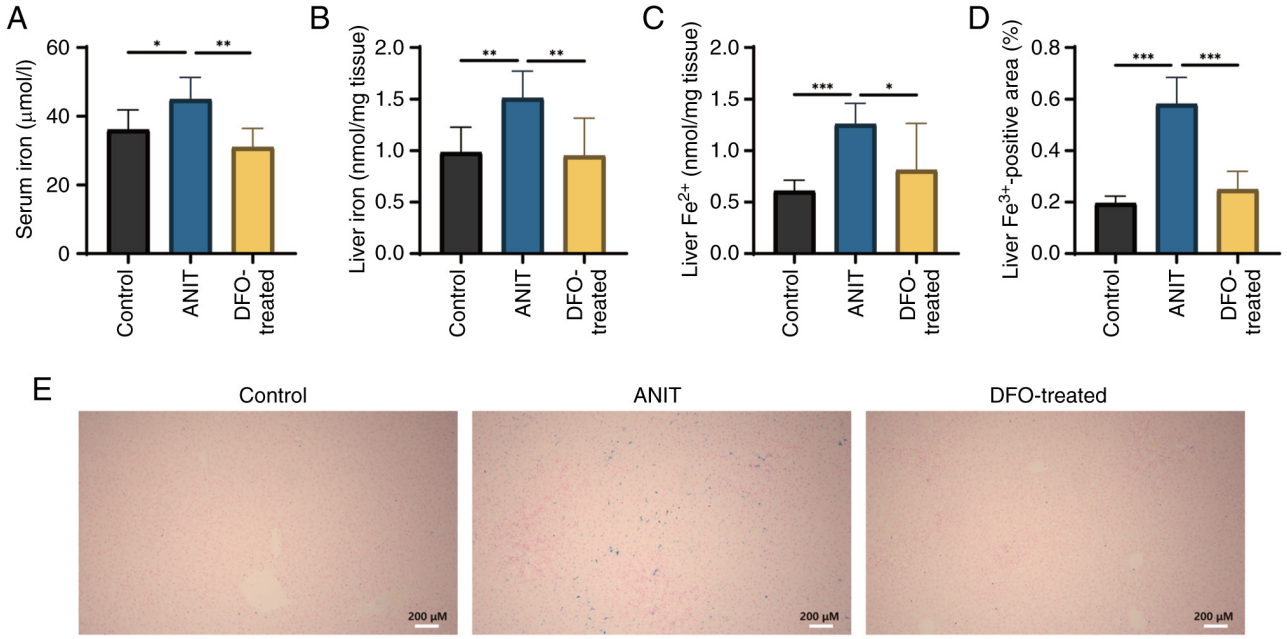

Figure 4. Free iron ions are aberrantly increased in serum and liver samples from rats with chronic cholestasis. Control group was fed a chow diet, whereas ANIT and DFO-treated groups were intragastrically administered ANIT olive oil solution with or without DFO (n=8/group). (A) Serum iron, (B) liver iron and (C) liver Fe^{2+} levels were detected. (D) Liver Prussian blue Fe^{3+} positive area. Data are presented as the mean ± SD. P-values were determined by one-way ANOVA. *P<0.05, **P<0.01, ***P<0.001. (E) Prussian blue staining (scale bar, 200 μm). ANIT, α-naphthyl isothiocyanate; DFO, deferoxamine.

(Fig. 6A-F). DFO treatment notably increased the expression of Nrf2, XCT and GPX4, decreased Keap1 expression and further enhanced HO-1 expression. Similarly, the protein expression levels of liver FPN1 and FTH1 were significantly decreased, whereas those of TFR1, DMT1 and Steap3 were elevated in cholestasis-affected rats (Fig. 6G-L). DFO treatment effectively normalized these disruptions in the expression of iron metabolism-related proteins.

Discussion

Cholestasis is a pathological condition that suppresses bile formation and excretion, which is influenced by various factors affecting the liver (29). During cholestatic liver disease progression, sustained cholestasis can trigger inflammation in bile duct cells and hepatocytes (30). This inflammatory response can then prompt immune cells to generate abundant ROS in the presence of proinflammatory factors to combat pathogens. However, failure to promptly eliminate the excessive ROS results in their accumulation, serving as a pathogenic stimulus to culminate in hepatocyte cell death (12).

A hallmark of ferroptosis is the decreased uptake of intracellular cystine and synthesis of cysteine, which limits GSH biosynthesis and reduces GSH-PX activity (31). GSH and GSH-PX scavenge free radicals and ROS-induced lipid peroxides *in vivo*, thereby mitigating oxidative damage within the organism (32,33). MDA is a primary toxic byproduct of lipid peroxidation, serving as an indicator of tissue peroxidative damage (34). Serum and liver tissue total iron, in addition to Fe^{2+} and Fe^{3+} levels, indicate potential iron overload in the organism. Excess free Fe^{2+} reacts with intracellular H_2O_2 through the Fenton reaction, producing Fe^{3+} and potent oxidants. These oxidants damage cell membranes and facilitate cellular ferroptosis. Strong oxidants can damage cell membranes and induce ferroptosis (14). As described in previous studies (13,35), transmission electron microscopy hallmarks of ferroptosis include hepatocyte mitochondria with reduced size, increased bilayer density, ruptured and crumpled outer membranes, and diminished or absent cristae, whilst the nuclei remain intact. Consistent with these established features, our ultrastructural analysis revealed characteristic mitochondrial abnormalities in cholestatic rats, including reduced size, blurred and fused cristae, and increased bilayer membrane density), supporting the occurrence of ferroptosis in our model. ASCL4 and COX2 are key proteins involved in detecting ferroptosis. ASCL4 catalyzes the formation of polyunsaturated fatty acid-acyl coenzyme A derivatives (36), which bind to phospholipids in cell membranes through the action of lysophosphatidylcholine acyltransferase 3, increasing membrane susceptibility to oxidation and lipid peroxide-induced damage (37,38). By contrast, COX2 enhances nicotinamide adenine dinucleotide phosphate oxidase 1-mediated lipid peroxidation to elevate intracellular ROS levels (39).

In the present study, rats with chronic cholestasis exhibited significantly reduced GSH content and GSH-PX activity, alongside a marked increase in MDA content in liver tissue, indicating a severe deficiency in antioxidant capacity and substantial lipid peroxidation damage due to lipid peroxide accumulation. Total serum iron, total iron and Fe^{2+} levels in liver tissue were significantly elevated in these model rats. Prussian blue staining revealed extensive blue staining in liver tissue, signifying abnormal iron accumulation, particularly Fe^{3+}, in cholestatic rats. Transmission electron microscopy also demonstrated indistinct hepatocyte boundaries, intact nuclei, reduced mitochondrial size, blurred and fused mitochondrial cristae, with increased bilayer membrane density. These

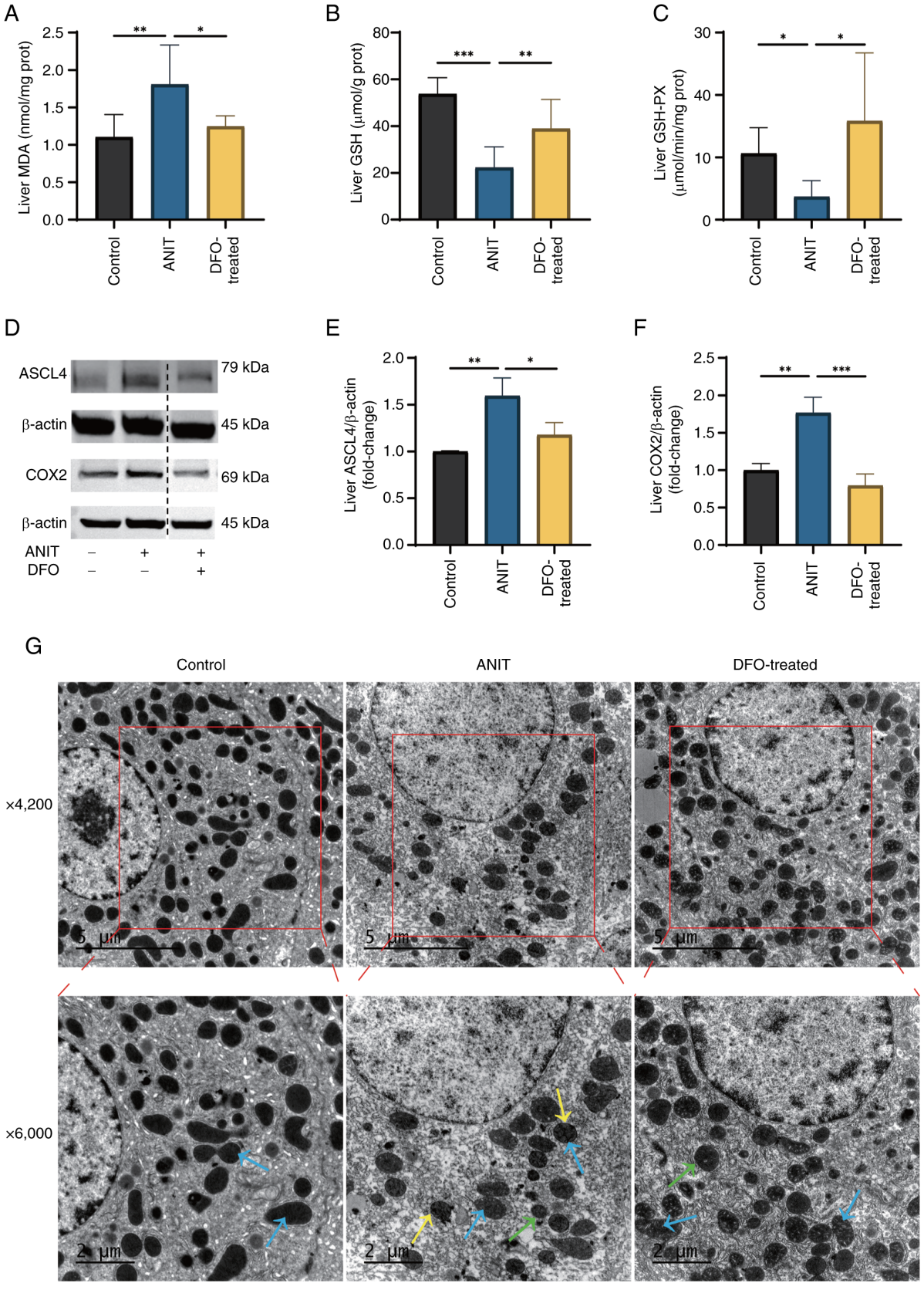

Figure 5. Levels of lipid peroxidation and ferroptosis markers are increased in the liver of rats with chronic cholestasis and the liver ultrastructure is affected in a DFO-reversible manner. Control group was fed a chow diet, whereas ANIT and DFO-treated groups were intragastrically administered ANIT olive oil solution with or without DFO (n=8/group). Levels of (A) MDA, (B) GSH and (C) GSH-PX were detected. (D) Changes in ferroptosis marker protein expression. The blots shown are representative of three independent experiments. A dotted line indicates that the lanes were non-adjacent on the original gel. All target protein bands and their corresponding loading control bands shown side-by-side were derived from the same membrane. Relative expression levels of (E) ASCL4 and (F) COX2. Data are presented as the mean ± SD. P-values were determined by one-way ANOVA. *P<0.05, **P<0.01, ***P<0.001. (G) Transmission electron microscope sections, blue arrows indicate mitochondrial cristae, yellow arrows indicate outer mitochondrial membrane and green arrows point to mitochondria (scale bars, 5 and 2 μm). DFO, deferoxamine; ANIT, α-naphthyl isothiocyanate; MDA, malondialdehyde; GSH, glutathione; GSH-PX, glutathione peroxidase; ASCL4, acyl-CoA synthetase long-chain family member 4; COX2, cyclooxygenase 2.

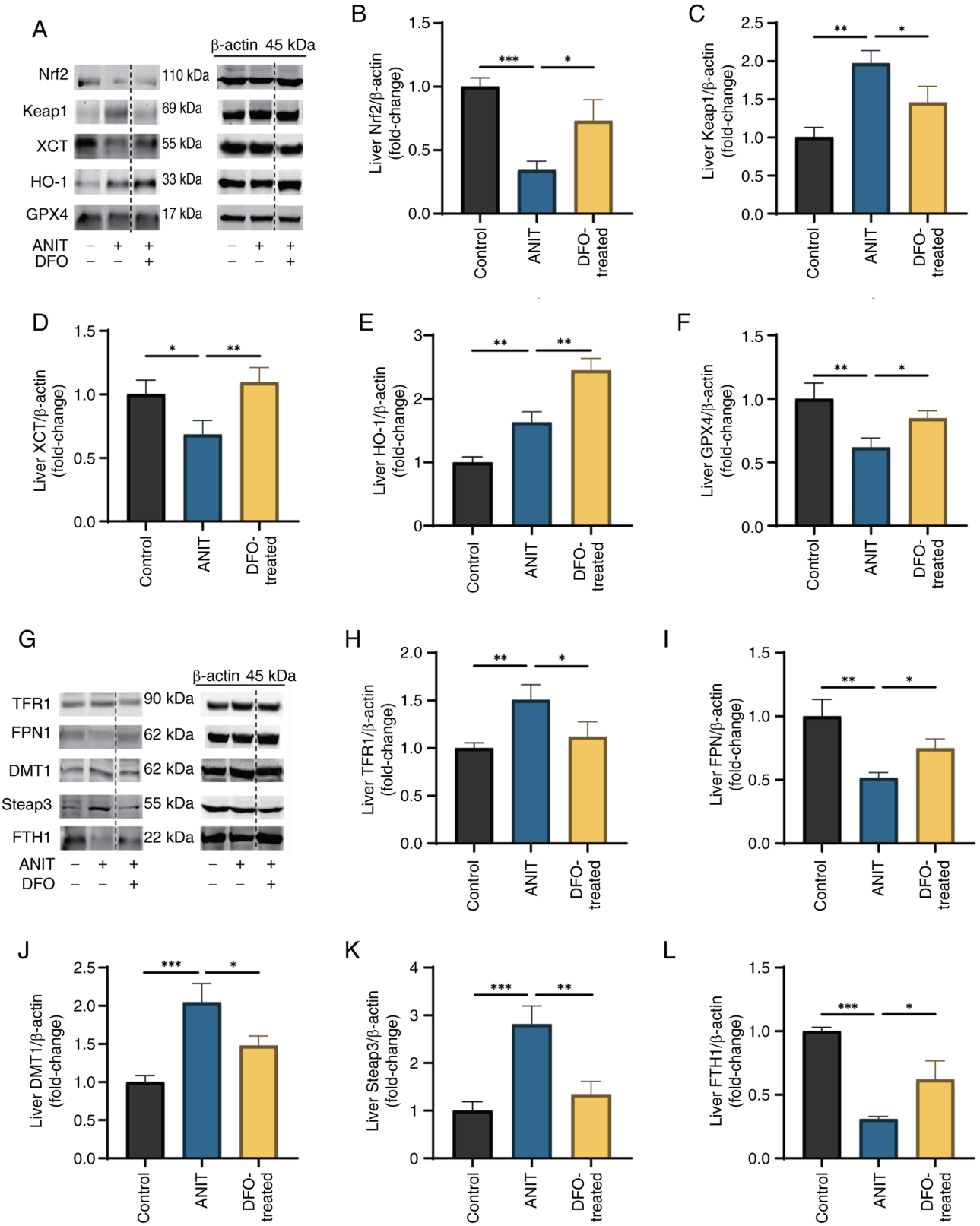

Figure 6. Abnormal expression of antioxidant and iron metabolism-related proteins in liver samples of rats with chronic cholestasis. Control group was fed a chow diet, whereas the ANIT and DFO-treated groups were intragastrically administered ANIT olive oil solution with or without DFO (n=8/group). (A) Changes in ferroptosis antioxidant-related protein expression. The blots shown are representative of three independent experiments. A dotted line indicates that the lanes were non-adjacent on the original gel. All target protein bands and their corresponding loading control bands shown side-by-side were derived from the same membrane. Relative expression levels of (B) Nrf2, (C) Keap1, (D) XCT, (E) HO-1 and (F) GPX4. (G) Changes in iron metabolism-related protein expression. The blots shown are representative of three independent experiments. A dotted line indicates that the lanes were non-adjacent on the original gel. All target protein bands and their corresponding loading control bands shown side-by-side were derived from the same membrane. Relative expression levels of (H) TFR1, (I) FPN1, (J) DMT1, (K) Steap3 and (L) FTH1. Data are presented as the mean ± SD. P-values were determined by one-way ANOVA. *P<0.05, **P<0.01, ***P<0.001. ANIT, α-naphthyl isothiocyanate; DFO, deferoxamine; Nrf2, nuclear factor erythroid-2-related factor 2; Keap1, Kelch-like ECH-associated protein 1, XCT, cystine/glutamate transporter; HO-1, heme oxygenase 1; GPX4, glutathione peroxidase 4; TFR1, transferrin receptor 1; FPN1, ferroportin 1; DMT1, divalent metal transporter 1; Steap3, six-transmembrane epithelial antigen of the prostate 3; FTH1, ferritin heavy chain 1.

ultrastructural and morphological alterations in hepatocytes align with the characteristics of ferroptosis. Western blotting revealed markedly increased expression levels of ASCL4 and COX2 in the liver tissue of model rats, signifying a substantial rise in lipid peroxide levels and the occurrence of ferroptosis. These findings suggest that ferroptosis of hepatocytes may occur during ANIT-induced chronic cholestasis in rats.

Although the present study was conducted in an animal model, the relevance of ferroptosis to human cholestatic liver diseases has been recognized. Previous studies have reported iron accumulation and dysregulation of ferroptosis-related genes (such as GPX4 and SLC7A11) in liver tissues from patients with intrahepatic cholestasis of pregnancy or cholestatic drug-induced liver injury (40,41). This converging evidence suggests that the ferroptotic pathway identified in the present study may have translational importance in human cholestatic conditions.

In the ferroptosis antioxidant pathway, System Xc- is comprised of two proteins, XCT and 4F2 cell-surface antigen heavy chain, facilitating a 1:1 exchange of extracellular cystine for intracellular glutamate (42). Cystine serves as a vital precursor for intracellular cysteine synthesis, positioning XCT as a key component in this pathway. GPX4 is a selenoprotein that reduces lipid peroxides to lipid alcohols, thereby preventing ferroptosis by scavenging excess intracellular lipid peroxides. This enzyme is the most potent antioxidant enzyme in the GPX family, which serves as a pivotal target within the antioxidant pathway (43). The Keap1/Nrf2/HO-1 axis constitutes a key intracellular antioxidant pathway (44). Keap1 inhibits Nrf2 by retaining it in the cytoplasm (45), thereby preventing its nuclear translocation and subsequent antioxidant activity (46). Nrf2 is a central component in the antioxidant system, regulating the upstream factor HO-1 (47), which enhances the expression of both HO-1 and GPX4 (48). HO-1 exhibits antioxidant and anti-inflammatory properties, mitigating mitochondrial and lipid peroxidation damage (49).

In the present study, Keap1 protein expression was elevated, whereas XCT, GPX4 and Nrf2 protein expression levels were reduced, in the liver tissues of rats following ANIT-induced chronic cholestasis. This indicated that the System Xc- transporter was inhibited during cholestasis, resulting in cysteine deficiency and limited GPX4 synthesis, which failed to efficiently scavenge excessive ROS. The Keap1/Nrf2/HO-1 pathway was suppressed, impairing antioxidant activity. The observed upregulation of HO-1 in the present model appeared paradoxical to the overall suppression of the Nrf2 axis. However, this can be interpreted as a compensatory stress response to severe oxidative injury. The initial induction of HO-1 may represent the attempt of the liver to mitigate damage. In the face of sustained cholestatic insult, this compensatory mechanism ultimately proved insufficient to prevent the progression of ferroptosis, as evidenced by the downregulation of other key antioxidants, such as GPX4 (50,51). Consequently, the antioxidant capacity of the body was diminished and excessive intracellular lipid peroxides were not effectively eliminated, leading to ferroptosis.

In the iron metabolism pathway, TFR1 on the cell membrane facilitates the intracellular transport of iron ions by binding to the extracellular Tf-Fe complex (52). Steap3 reduces transferrin-bound Fe^{3+} to Fe^{2+} (53), which is then translocated into the intracytoplasmic labile iron pool (LIP) through DMT1. DMT1 is crucial for the intracellular transport of ferric ions and serves as an essential metal ion transporter in the iron metabolism pathway (54). Cytoplasmic ferritin as a multimer can decrease intracellular free iron ion levels by binding to free iron ions in the LIP. FPN is the sole protein facilitating iron efflux in mammals, enabling the transfer of iron ions out of cells and thereby reducing intracellular free iron ion concentrations (55). The mechanism of iron-induced cell death is illustrated in Fig. 7.

The present study revealed that in liver tissues of rats after ANIT-induced chronic cholestasis, TFR1, Steap3 and DMT1 protein expression increased, whereas FTH1 and FPN1 expression decreased. This suggests that cholestasis can enhance cellular iron ion uptake, reduce ferritin storage function, diminish iron exclusion capacity, elevate intracellular free iron levels, intensify the Fenton reaction and promote excessive ROS, leading to lipid peroxidation and ferroptosis in hepatocytes.

In summary, these aforementioned observations suggested that decreased antioxidant and iron metabolism in hepatocytes, resulting in iron-induced cell death, is a key pathological mechanism in chronic cholestasis.

DFO is a potent iron chelator that is extensively used in clinical settings to treat iron overload disorders such as β-thalassemia and myelodysplastic syndrome (24). In the present study, the protective effect of DFO was shown to be primarily mediated through its capacity to chelate iron. DFO treatment significantly reduced serum and hepatic total iron levels as well as Fe^{2+} content, and markedly decreased hepatic iron deposition. Furthermore, DFO alleviated indices of iron-dependent oxidative damage, including lowering lipid peroxidation (MDA) and restoring antioxidant capacity (GSH and GSH-PX). In addition, DFO normalized the expression of key proteins involved in iron metabolism (TFR1, FPN1, etc., Fig. 6G-L) and ferroptosis (ASCL4, COX2). By reducing intracellular and systemic iron load, DFO can limit the substrates available for the Fenton reaction (56), thereby decreasing the generation of hydroxyl radicals and subsequent lipid peroxidation (57,58). This reduction in iron-driven oxidative stress ultimately mitigates the process of ferroptosis (59).

The present study investigated the role of the ferroptosis inhibitor DFO in addressing ANIT-induced chronic cholestasis in rats, aiming to test the hypothesis that hepatocellular ferroptosis is a key pathogenic mechanism in chronic cholestasis and that targeting it may be therapeutic. The findings indicated that DFO may markedly ameliorate cholestasis. Biochemically, DFO reduced serum levels of TBA, TBIL, DBIL, LDL and TCH, decreased GGT, ALP and ALT activities, increased serum TG levels and mitigated hepatocyte dysfunction in cholestatic rats. In hepatic tissues, DFO enhanced GSH content and GSH-PX activity, boosted antioxidant capacity, lowered MDA content, reduced lipid peroxidation and decreased HYP content in the liver of model rats. Biochemical analysis demonstrated that DFO effectively reduced serum total iron, liver tissue total iron and Fe^{2+} levels in model rats. Hepatic histopathology revealed that DFO decreased small bile duct proliferation in the hepatic portal areas, reduced inflammatory cell infiltration and diminished

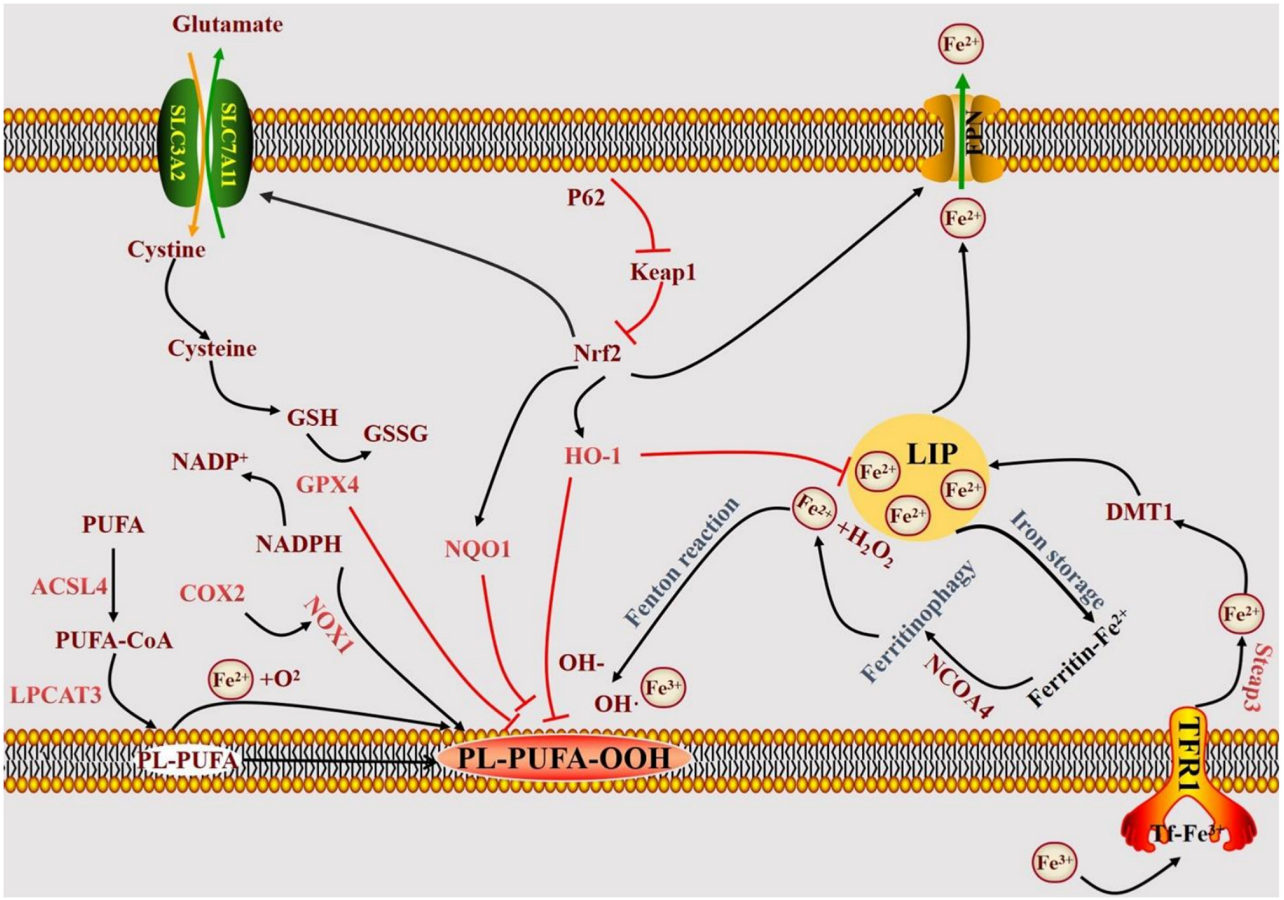

Figure 7. Diagram of the mechanism of ferroptosis. ASCL4, acyl-CoA synthetase long-chain family member 4; COX2, cyclooxygenase 2; DMT1, divalent metal transporter 1; FPN, ferroportin; GSSG, oxidized glutathione; GPX4, glutathione peroxidase 4; GSH, glutathione; HO-1, heme oxygenase 1; Keap1, Kelch-like ECH-associated protein 1; LIP, labile iron pool; LPCAT3, lysophosphatidylcholine acyltransferase 3; NCOA4, nuclear receptor coactivator 4; NOX1, nicotinamide adenine dinucleotide phosphate oxidase 1; NQO1, NAD(P)H quinone dehydrogenase 1; Nrf2, nuclear factor erythroid-2-related factor 2; PL-PUFA-OOH, phospholipid-polyunsaturated fatty acid hydroperoxide; SLC7A11, solute carrier family 7 member 11; Steap3, six-transmembrane epithelial antigen of the prostate 3; TFR1, transferrin receptor 1.

collagen fiber deposition and Fe^{3+} accumulation. Transmission electron microscopy indicated that hepatocyte nuclei in the DFO group remained intact, with normal mitochondrial morphology, size and clear cristae. Western blotting showed that DFO downregulated the protein expression of α-SMA, a classical marker of activated HSCs, in the rat liver tissue, indicating the inhibition of HSC activation. This contributed to the deceleration of hepatic fibrosis progression in cholestasis. DFO downregulated ASCL4 and COX2 protein expression in liver tissues, and inhibited ANIT-induced ferroptosis in chronically cholestatic rats. After intervention, DFO reduced Keap1, TFR1, DMT1 and Steap3 protein levels, whereas it upregulated Nrf2, XCT, HO-1, GPX4, FPN1 and FTH1 in liver tissues. This suggested that DFO can mitigate ferroptosis by enhancing hepatocyte iron storage and excretion, reducing extracellular ferric iron translocation and decreasing free ferric iron content, thereby boosting antioxidant capacity and preventing ferroptosis.

However, it is important to acknowledge that DFO is a pleiotropic agent with biological effects beyond iron chelation. These include intrinsic antioxidant properties and potential modulatory effects on non-parenchymal cells, such as HSCs (60,61). While the present data strongly supported iron chelation as the primary mechanism, the contribution of these additional pleiotropic effects to the overall hepatoprotection observed cannot be ruled out.

The present study has several limitations. The findings are based on a single animal model of cholestasis. Validation in additional models would strengthen the generalizability of the conclusions. In addition, the use of DFO, though effective, prevents the unequivocal attribution of all protective effects solely to the reduction of ferroptosis through iron chelation, due to its pleiotropic nature. Future studies using more specific ferroptosis inhibitors (such as ferrostatin-1) (62) or genetic approaches to manipulate key ferroptosis regulators (including GPX4) would be invaluable. The lack of *in vitro* data also limited the mechanistic depth. Establishing *in vitro* models of bile acid-induced hepatocyte injury will be essential for dissecting the precise molecular sequence of events.

In conclusion, the present findings demonstrated that ferroptosis, driven by the concurrent disruption of hepatocyte antioxidant and iron metabolism capacities, is a key pathological mechanism in chronic cholestasis. The iron chelator DFO alleviated cholestatic liver injury, an effect likely mediated by the reduction of iron overload and the subsequent ferroptotic process. The present study highlighted the ferroptosis pathway as a promising therapeutic target for cholestatic liver diseases.

Acknowledgements

Not applicable.

Funding

The present study was funded by the National Natural Science Foundation of China (grant no. 81774196), the Natural Science Foundation of Shanghai Municipality of China (grant no. 22ZR1459200) and the Luzhou Science and Technology Innovation City Development Fund of China (grant no. 2024RQN226).

Availability of data and materials

The data generated in the present study may be requested from the corresponding author.

Authors' contributions

XW designed the present study. ZG performed experiments. JW performed data interpretation. YW performed data analysis. XL, YX, LQ, JL and PL assisted in collecting the samples. All authors read and approved the final manuscript. XW and ZG confirm the authenticity of all the raw data.

Ethics approval and consent to participate

The animal protocol was approved by the Animal Care and Utilization Committee of Shanghai University of Traditional Chinese Medicine (Ethics Review Number: PZSHUTCM210715019) and was conducted following the Guide for the Care and Use of Laboratory Animals (26).

Patient consent for publication

Not applicable.

Competing interests

The authors declare that they have no competing interests.

References

1. Karpen SJ, Kelly D, Mack C and Stein P: Ileal bile acid transporter inhibition as an anticholestatic therapeutic target in biliary atresia and other cholestatic disorders. Hepatol Int 14: 677-689, 2020.
2. Pollock G and Minuk GY: Diagnostic considerations for cholestatic liver disease. J Gastroenterol Hepatol 32: 1303-1309, 2017.
3. Bortolini M, Almasio P, Bray G, Budillon G, Coltorti M, Frezza M, Okolicsanyi L, Salvagnini M and Williams R: Multicentre survey of the prevalence of intrahepatic cholestasis in 2520 consecutive patients with newly diagnosed chronic liver disease. Drug Invest 4 (Suppl 4): S83-S89, 1992.
4. Xie W, Cao Y, Xu M, Wang J, Zhou C, Yang X, Geng X, Zhang W, Li N and Cheng J: Prognostic significance of elevated cholestatic enzymes for fibrosis and hepatocellular carcinoma in hospital discharged chronic viral hepatitis patients. Sci Rep 7: 10289, 2017.
5. Ibrahim SH, Kamath BM, Loomes KM and Karpen SJ: Cholestatic liver diseases of genetic etiology: Advances and controversies. Hepatology 75: 1627-1646, 2022.
6. Dixon SJ, Lemberg KM, Lamprecht MR, Skouta R, Zaitsev EM, Gleason CE, Patel DN, Bauer AJ, Cantley AM, Yang WS, *et al*: Ferroptosis: An iron-dependent form of nonapoptotic cell death. Cell 149: 1060-1072, 2012.
7. Bayir H, Dixon SJ, Tyurina YY, Kellum JA and Kagan VE: Ferroptotic mechanisms and therapeutic targeting of iron metabolism and lipid peroxidation in the kidney. Nat Rev Nephrol 19: 315-336, 2023.
8. Yang W: Iron turns to wild when the transferrin is away. Blood 136: 649-650, 2020.
9. Buckley CD, Barone F, Nayar S, Benezech C and Caamano J: Stromal cells in chronic inflammation and tertiary lymphoid organ formation. Annu Rev Immunol 33: 715-745, 2015.
10. Forrester SJ, Kikuchi DS, Hernandes MS, Xu Q and Griendling KK: Reactive oxygen species in metabolic and inflammatory signaling. Circ Res 122: 877-902, 2018.
11. Zhang WB, Yang F, Wang Y, Jiao FZ, Zhang HY, Wang LW and Gong ZJ: Inhibition of HDAC6 attenuates LPS-induced inflammation in macrophages by regulating oxidative stress and suppressing the TLR4-MAPK/NF-κB pathways. Biomed Pharmacother 117: 109166, 2019.
12. Xie Y, Hou W, Song X, Yu Y, Huang J, Sun X, Kang R and Tang D: Ferroptosis: Process and function. Cell Death Differ 23: 369-379, 2016.
13. Han C, Liu Y, Dai R, Ismail N, Su W and Li B: Ferroptosis and its potential role in human diseases. Front Pharmacol 11: 239, 2020.
14. Wang Y and Tang M: PM2.5 induces ferroptosis in human endothelial cells through iron overload and redox imbalance. Environ Pollut 254: 112937, 2019.
15. Jiang X, Stockwell BR and Conrad M: Ferroptosis: Mechanisms, biology and role in disease. Nat Rev Mol Cell Biol 22: 266-282, 2021.
16. Lyberopoulou A, Chachami G, Gatselis NK, Kyratzopoulou E, Saitis A, Gabeta S, Eliades P, Paraskeva E, Zachou K, Koukoulis GK, *et al*: Low serum hepcidin in patients with autoimmune liver diseases. PLoS One 10: e0135486, 2015.
17. Marques O, Horvat NK, Zechner L, Colucci S, Sparla R, Zimmermann S, Neufeldt CJ, Altamura S, Qiu R, Mudder K, *et al*: Inflammation-driven NF-kappab signaling represses ferroportin transcription in macrophages via HDAC1 and HDAC3. Blood 145: 866-880, 2025.
18. Xie X, Chang L, Zhu X, Gong F, Che L, Zhang R, Wang L, Gong C, Fang C, Yao C, *et al*: Rubiadin mediates the upregulation of hepatic hepcidin and alleviates iron overload via BMP6/SMAD1/5/9-signaling pathway. Int J Mol Sci 26: 1385, 2025.
19. Delesderrier E, Monteiro JDC, Freitas S, Pinheiro IC, Batista MS and Citelli M: Can iron and polyunsaturated fatty acid supplementation induce ferroptosis? Cell Physiol Biochem 57: 24-41, 2023.
20. Liu C, Liu Z, Dong Z, Liu S, Kan H and Zhang S: Multifaceted interplays between the essential players and lipid peroxidation in ferroptosis. J Genet Genomics 52: 1071-1081, 2025.
21. Tsuchida T and Friedman SL: Mechanisms of hepatic stellate cell activation. Nat Rev Gastroenterol Hepatol 14: 397-411, 2017.
22. Yu Y, Jiang L, Wang H, Shen Z, Cheng Q, Zhang P, Wang J, Wu Q, Fang X, Duan L, *et al*: Hepatic transferrin plays a role in systemic iron homeostasis and liver ferroptosis. Blood 136: 726-739, 2020.
23. Zhang Q, Qu Y, Zhang Q, Li F, Li B, Li Z, Dong Y, Lu L and Cai X: Exosomes derived from hepatitis b virus-infected hepatocytes promote liver fibrosis via mir-222/TFRC axis. Cell Biol Toxicol 39: 467-481, 2023.
24. Yang L, Xie P, Wu J, Yu J, Li X, Ma H, Yu T, Wang H, Ye J, Wang J and Zheng H: Deferoxamine treatment combined with sevoflurane postconditioning attenuates myocardial ischemia-reperfusion injury by restoring HIF-1/BNIP3-mediated mitochondrial autophagy in GK rats. Front Pharmacol 11: 6, 2020.
25. Duscher D, Neofytou E, Wong VW, Maan ZN, Rennert RC, Inayathullah M, Januszyk M, Rodrigues M, Malkovskiy AV, Whitmore AJ, *et al*: Transdermal deferoxamine prevents pressure-induced diabetic ulcers. Proc Natl Acad Sci USA 112: 94-99, 2015.
26. National RCUC: Guide for the Care and Use of Laboratory Animals. National Academies Press, Washington, DC, 2011.
27. Liu X, Wang J, Li M, Qiu J, Li X, Qi L, Liu J, Liu P, Xie G and Wang X: Farnesoid x receptor is an important target for the treatment of disorders of bile acid and fatty acid metabolism in mice with nonalcoholic fatty liver disease combined with cholestasis. J Gastroenterol Hepatol 38: 1438-1446, 2023.

28. Wang H, Jiang C, Yang Y, Li J, Wang Y, Wang C and Gao Y: Resveratrol ameliorates iron overload induced liver fibrosis in mice by regulating iron homeostasis. PeerJ 10: e13592, 2022.
29. Xiang D, Liu Y, Zu Y, Yang J, He W, Zhang C and Liu D: Calculus bovis sativus alleviates estrogen cholestasis-induced gut and liver injury in rats by regulating inflammation, oxidative stress, apoptosis, and bile acid profiles. J Ethnopharmacol 302: 115854, 2023.
30. Zhuang Y, Ortega-Ribera M, Thevkar Nagesh P, Joshi R, Huang H, Wang Y, Zivny A, Mehta J, Parikh SM and Szabo G: Bile acid-induced IRF3 phosphorylation mediates cell death, inflammatory responses, and fibrosis in cholestasis-induced liver and kidney injury via regulation of ZBP1. Hepatology 79: 752-767, 2024.
31. Yang WS and Stockwell BR: Ferroptosis: Death by lipid peroxidation. Trends Cell Biol 26: 165-176, 2016.
32. Alajbeg IZ, Lapic I, Rogic D, Vuletic L, Andabak Rogulj A, Illes D, Knezović Zlatarić D, Badel T, Vrbanovic E and Alajbeg I: Within-subject reliability and between-subject variability of oxidative stress markers in saliva of healthy subjects: A longitudinal pilot study. Dis Markers 2017: 2697464, 2017.
33. Hakkoymaz H, Nazik S, Seyithanoglu M, Guler O, Sahin AR, Cengiz E and Yazar FM: The value of ischemia-modified albumin and oxidative stress markers in the diagnosis of acute appendicitis in adults. Am J Emerg Med 37: 2097-2101, 2019.
34. Tangvarasittichai S: Oxidative stress, insulin resistance, dyslipidemia and type 2 diabetes mellitus. World J Diabetes 6: 456-480, 2015.
35. Moore DD, Kato S, Xie W, Mangelsdorf DJ, Schmidt DR, Xiao R and Kliewer SA: International union of pharmacology. LXII. The NR1h and NR1i receptors: Constitutive androstane receptor, pregnene x receptor, farnesoid x receptor alpha, farnesoid x receptor beta, liver x receptor alpha, liver x receptor beta, and vitamin d receptor. Pharmacol Rev 58: 742-759, 2006.
36. Kagan VE, Mao G, Qu F, Angeli JP, Doll S, Croix CS, Dar HH, Liu B, Tyurin VA, Ritov VB, *et al*: Oxidized arachidonic and adrenic PEs navigate cells to ferroptosis. Nat Chem Biol 13: 81-90, 2017.
37. Doll S, Proneth B, Tyurina YY, Panzilius E, Kobayashi S, Ingold I, Irmler M, Beckers J, Aichler M, Walch A, *et al*: ACSL4 dictates ferroptosis sensitivity by shaping cellular lipid composition. Nat Chem Biol 13: 91-98, 2017.
38. Yang WS, Kim KJ, Gaschler MM, Patel M, Shchepinov MS and Stockwell BR: Peroxidation of polyunsaturated fatty acids by lipoxygenases drives ferroptosis. Proc Natl Acad Sci USA 113: E4966-E4975, 2016.
39. Daiber A, Di Lisa F, Oelze M, Kroller-Schon S, Steven S, Schulz E and Munzel T: Crosstalk of mitochondria with NADPH oxidase via reactive oxygen and nitrogen species signalling and its role for vascular function. Br J Pharmacol 174: 1670-1689, 2017.
40. You Y, Qian Z, Jiang Y, Chen L, Wu D, Liu L, Zhang F, Ning X, Zhang Y and Xiao J: Insights into the pathogenesis of gestational and hepatic diseases: The impact of ferroptosis. Front Cell Dev Biol 12: 1482838, 2024.
41. Teschke R: Treatment of drug-induced liver injury. Biomedicines 11: 15, 2022.
42. Lewerenz J, Hewett SJ, Huang Y, Lambros M, Gout PW, Kalivas PW, Massie A, Smolders I, Methner A, Pergande M, *et al*: The cystine/glutamate antiporter system x(c)(-) in health and disease: From molecular mechanisms to novel therapeutic opportunities. Antioxid Redox Signal 18: 522-555, 2013.
43. Kan X, Yin Y, Song C, Tan L, Qiu X, Liao Y, Liu W, Meng S, Sun Y and Ding C: Newcastle-disease-virus-induced ferroptosis through nutrient deprivation and ferritinophagy in tumor cells. iScience 24: 102837, 2021.
44. Sun X, Ou Z, Chen R, Niu X, Chen D, Kang R and Tang D: Activation of the p62-keap1-NRF2 pathway protects against ferroptosis in hepatocellular carcinoma cells. Hepatology 63: 173-184, 2016.
45. Yoo S, Kim M, Bae JY, Lee SA and Koh G: Bardoxolone methyl inhibits ferroptosis through the Keap1-Nrf2 pathway in renal tubular epithelial cells. Mol Med Rep 32: 267, 2025.
46. Ichimura Y, Waguri S, Sou YS, Kageyama S, Hasegawa J, Ishimura R, Saito T, Yang Y, Kouno T, Fukutomi T, *et al*: Phosphorylation of p62 activates the Keap1-Nrf2 pathway during selective autophagy. Mol Cell 51: 618-631, 2013.
47. Chen Y, Ma L, Yan Y, Wang X, Cao L, Li Y and Li M: Ophiopogon japonicus polysaccharide reduces doxorubicin-induced myocardial ferroptosis injury by activating Nrf2/GPX4 signaling and alleviating iron accumulation. Mol Med Rep 31: 36, 2025.
48. Xiao P, Huang H, Zhao H, Liu R, Sun Z, Liu Y, Chen N and Zhang Z: Edaravone dexborneol protects against cerebral ischemia/reperfusion-induced blood-brain barrier damage by inhibiting ferroptosis via activation of nrf-2/HO-1/GPX4 signaling. Free Radic Biol Med 217: 116-125, 2024.
49. Hu T, Wei G, Xi M, Yan J, Wu X, Wang Y, Zhu Y, Wang C and Wen A: Synergistic cardioprotective effects of danshensu and hydroxysafflor yellow a against myocardial ischemia-reperfusion injury are mediated through the Akt/Nrf2/HO-1 pathway. Int J Mol Med 38: 83-94, 2016.
50. Lin Q, Li S, Jin H, Cai H, Zhu X, Yang Y, Wu J, Qi C, Shao X, Li J, *et al*: Mitophagy alleviates cisplatin-induced renal tubular epithelial cell ferroptosis through ROS/HO-1/GPX4 axis. Int J Biol Sci 19: 1192-1210, 2023.
51. Choi AM and Alam J: Heme oxygenase-1: Function, regulation, and implication of a novel stress-inducible protein in oxidant-induced lung injury. Am J Respir Cell Mol Biol 15: 9-19, 1996.
52. Fisher AL, Wang CY, Xu Y, Joachim K, Xiao X, Phillips S, Moschetta GA, Alfaro-Magallanes VM and Babitt JL: Functional role of endothelial transferrin receptor 1 in iron sensing and homeostasis. Am J Hematol 97: 1548-1559, 2022.
53. Deng P, Li J, Lu Y, Hao R, He M, Li M, Tan M, Gao P, Wang L, Hong H, *et al*: Chronic cadmium exposure triggered ferroptosis by perturbing the STEAP3-mediated glutathione redox balance linked to altered metabolomic signatures in humans. Sci Total Environ 905: 167039, 2023.
54. Gao X, Hu W, Qian D, Bai X, He H, Li L and Sun S: The mechanisms of ferroptosis under hypoxia. Cell Mol Neurobiol 43: 3329-3341, 2023.
55. Nairz M, Fritsche G, Brunner P, Talasz H, Hantke K and Weiss G: Interferon-gamma limits the availability of iron for intramacrophage salmonella typhimurium. Eur J Immunol 38: 1923-1936, 2008.
56. Ge W, Jie J, Yao J, Li W, Cheng Y and Lu W: Advanced glycation end products promote osteoporosis by inducing ferroptosis in osteoblasts. Mol Med Rep 25: 140, 2022.
57. Chen GH, Song CC, Pantopoulos K, Wei XL, Zheng H and Luo Z: Mitochondrial oxidative stress mediated Fe-induced ferroptosis via the NRF2-ARE pathway. Free Radic Biol Med 180: 95-107, 2022.
58. Holden P and Nair LS: Deferoxamine: An angiogenic and antioxidant molecule for tissue regeneration. Tissue Eng Part B Rev 25: 461-470, 2019.
59. Zeng Z, Huang H, Zhang J, Liu Y, Zhong W, Chen W, Lu Y, Qiao Y, Zhao H, Meng X, *et al*: HDM induce airway epithelial cell ferroptosis and promote inflammation by activating ferritinophagy in asthma. FASEB J 36: e22359, 2022.
60. Mohammed A, Abd Al Haleem EN, El-Bakly WM and El-Demerdash E: Deferoxamine alleviates liver fibrosis induced by CCl4 in rats. Clin Exp Pharmacol Physiol 43: 760-768, 2016.
61. Liu MX, Gu YY, Nie WY, Zhu XM, Qi MJ, Zhao RM, Zhu WZ and Zhang XL: Formononetin induces ferroptosis in activated hepatic stellate cells to attenuate liver fibrosis by targeting NADPH oxidase 4. Phytother Res 38: 5988-6003, 2024.
62. Xie J, Ye Z, Li L, Xia Y, Yuan R, Ruan Y and Zhou X: Ferrostatin-1 alleviates oxalate-induced renal tubular epithelial cell injury, fibrosis and calcium oxalate stone formation by inhibiting ferroptosis. Mol Med Rep 26: 256, 2022.